Modeling microstructural evolution using atomic density function and effective pair potentials

Ji Hee Kim* and Stephen H. Garofalini
Department of Materials Science and Engineering, Rutgers University, 607 Taylor Road, Piscataway, New Jersey 08854, USA
(Received 30 April 2008; revised manuscript received 14 August 2008; published 28 October 2008)

We propose a numerical approach to the calculation of microstructural evolution in forms of the atomic density evolution. The modulation of the atomic density wave is driven by the minimization of the free-energy functional, which includes an effective pair potential term with softened core. As applications, we report simulation results of solidification, grain growth, and annealing for a one-component system in two dimensions.

DOI: 10.1103/PhysRevB.78.144109 PACS number(s): 61.50.Ah

I. INTRODUCTION

The microstructure of materials is a key factor in describing the materials' properties. Understanding the microstructural evolutions under different processing conditions are of interests to scientists and engineers in order to obtain the materials' properties for different applications. Mathematical modeling and computer simulations have also been studied for different time scales in order to describe this nonequilibrium microstructure at the atomic scale. Phase field crystal (PFC) is one of the recent models developed for simulating the evolution of the periodic modulation of atomic density. Elder *et al.*[1] have discussed PFC simulations and the dissipative dynamics of order parameters, which is calculated by the minimizing the free-energy functional. Compared with the conventional phase field simulation, the free-energy functional of PFC contains a higher order spacial gradient, which supports the description of the sharp modulation of atomic scale and the elastic-plastic properties of the materials from the symmetric nature of the high order gradients. With this model, crystal growth, elastic, and plastic deformations are simulated in diffusive time scales.[1] In order to describe specific materials, the coefficients of the gradient and its higher order terms are matched with elastic constants of the materials, and epitaxial growth, material hardness, phase reconstruction, and crack propagation are tested based on the relationship with the elastic properties of the materials.[2] As a method of incorporating the elastic interaction with better accuracy, the modified phase field crystal model is suggested.[3] This model describes the structural evolution not only on diffusive time scales (i.e., dislocation climbing, grain-boundary motion[4]) but also comparably "fast" phenomena, such as dislocation glide. Crystal structures, other than a triangular structure in two dimensions or body centered cubic (BCC) structure in three dimensions, are also studied with an external potential[5] or with nonvanishing terms in the free-energy functional.[2] As for the correlation function, the PFC model uses the three coefficients of the gradient terms which are a second-order series in Fourier space (or up to higher order in recent works for the three dimensional system, especially describing BCC structure[6]). Recently the idea of the density-functional theory (DFT) is adopted as correlation functions,[7–9] and this provides the links between the PFC method of diffusive time scale with DFT providing more accurate information about the materials. As technical improvements of the PFC method, renormalization-group (RG) theory is introduced in PFC calculations for expediting the simulation speed and enlarging the system size,[10,11] and the semi-implicit calculation is proposed for better accuracy.[12]

The simplified formulation of the phase field crystal approach for one-component system with only a pair potential contains three coefficients describing the pair correlations. It is analyzed that these coefficients are Fourier coefficients of the pair-correlation function and can be approximated using the pair potential at high temperature.[13] Khachaturyan and co-workers, in their atomic density functional (ADF) theory, removed the geometric restriction of the ADF Ising lattice model[14–16] and used a more complicated function in Fourier space giving exact periodicity over larger distance in real space.[13] Based on this approximation, instead of a pair-correlation function, we introduce the interatomic pair potential, i.e., Lennard-Jones potential with modification in the repulsive part. While the correlation function in PFC is based on the atomic structure and its elastic properties or compressibility, the pair potential that we use is based on the thermodynamic properties. The major benefit of using such a pair potential is not only that we include the thermodynamic properties but also that we do not need to predefine the atomic structure. The purpose of this work is introducing the simple pair potential in simulating the atomic densities to test the validity of the method in a qualitative way so that we can expand the usage of various types of more complicated and accurate interatomic potentials that are already available in the literature for such calculations. In the following sections, we give the theoretical description of the method and the related equations and demonstrate the simulation results and discuss.

II. THEORY

In this section, we describe the free-energy functional and the time evolution model of atomic density. Here we use the term "atomic density" in representing the atomic number density which is averaged over time. The free energy of a system with density modulation of atom $\rho(\vec{r})$ around the average density $\bar{\rho}$ is

$$F = \frac{1}{2}\int\int \delta\rho(\vec{r})W(\vec{r}-\vec{r}')\delta\rho(\vec{r}')d\vec{r}d\vec{r}' + k_BT\int\left(\rho(\vec{r})\ln\frac{\rho(\vec{r})}{\rho_l} - \delta\rho(\vec{r})\right)d\vec{r}, \quad (1)$$

where $\delta\rho(\vec{r})=\rho(\vec{r})-\bar{\rho}$ and ρ_l is the liquid density.[17] In Ref. 17 function W is the liquid state two-point correlation function. In our model, this term corresponds to the thermodynamic pairwise potential (by mean-field approximation, at high temperature[13]). The nonhomogeneous $\rho(\vec{r})$ is formed in favor of the effective pair potential term, i.e., $\int W(\vec{r}-\vec{r}')\delta\rho(\vec{r}')d\vec{r}'$, which prefers larger density around certain positions, while the second term of Eq. (1) prefers a uniform atomic density distribution and tends to suppress the increasing of the density modulation. The tradeoff between these two terms determines the $\rho(\vec{r})$. The free-energy change by the evolution of the density modulation is simplified using normalized density $d(\vec{r})=\delta\rho(\vec{r})/\bar{\rho}$ and expansion of the second term of the right-hand side of Eq. (1)

$$\frac{\Delta F}{\bar{\rho}} = \frac{\bar{\rho}}{2}\int\int d(\vec{r})W(\vec{r}-\vec{r}')d(\vec{r}')d\vec{r}d\vec{r}' + k_BT\int\left(\frac{1}{2}d^2(\vec{r}) - \frac{1}{6}d^3(\vec{r}) + \frac{1}{12}d^4(\vec{r}) - \cdots\right)d\vec{r}, \quad (2)$$

where $\Delta F=F-F_0$ and $F_0=F(\bar{\rho})$. In the next subsections, we compare the free energies of different structures with approximated atomic modulation in one and two dimensions and form the phase diagram.

A. Phase diagram

1. Stripe phase

In one-dimensional systems, possible structures are liquid and stripes. If we approximate the density modulation of the periodic state as one mode, i.e., $d(x)=A_{1s}\cos(qx)$, the relative free energy of the stripe phase is

$$\Delta F \approx \frac{\bar{\rho}}{2}A_{1s}^2\int\int \cos(qx)W(X)\cos[q(x+X)]dxdX + k_BT\int\left[\frac{1}{2}A_{1s}^2\cos^2(qx) - \frac{1}{6}A_{1s}^3\cos^3(qx) + \frac{1}{12}A_{1s}^4\cos^4(qx)\right]dx. \quad (3)$$

Then the free energy per unit length a is simplified as

$$\frac{\Delta F}{a\bar{\rho}} = \frac{1}{4}A_{1s}^2k_BT\left(1 - \frac{V_1\bar{\rho}}{k_BT} + \frac{1}{8}A_{1s}^2\right), \quad (4)$$

where

$$V_1 = -\int W(x)\cos(qx)dx. \quad (5)$$

This V_1 term is after all the zeroth order term of Fourier transform of the pair potential W. Minimizing F with respect to A_{1s} gives

$$A_{1s}^2 = 4\left(\frac{V_1\bar{\rho}}{k_BT} - 1\right), \quad (6)$$

and the minimum value of relative free-energy density is

$$\frac{\Delta F_{\min}}{a\bar{\rho}} = -\frac{1}{2}k_BT\left(\frac{V_1\bar{\rho}}{k_BT} - 1\right)^2. \quad (7)$$

Since A_{1s} is real,

$$\frac{\bar{\rho}V_1}{k_BT} \geq 1 \quad (8)$$

is the condition for the existence of this stripes phase.

In two dimensional, the density modulation of stripe phase can be simplified as $d(x,y)=A_{2s}\cos(qx)$. Relative free-energy density $\Delta F/a^2\bar{\rho}$, minimum value of $\Delta F/a^2\bar{\rho}$ and A_{2s} giving that minimum, and the $\bar{\rho}-T$ relation for the real amplitude of the density modulation have the same forms as the one-dimensional case while V_{2s} is taken place of V_{1s}. Here,

$$V_{2s} = -\int\int W(X,Y)\cos(qX)dXdY. \quad (9)$$

2. Triangular lattice

Triangular density modulation can be also simplified as one-mode wave, i.e., $d(x,y)=A_{2t}[\frac{1}{2}\cos(2qy/\sqrt{3}) - \cos(qx)\cos(qy/\sqrt{3})]$. Plugging this density profile into Eq. (2) gives relative free energy per unit area

$$\frac{F}{a^2\bar{\rho}} = \frac{3}{16}A_{2t}^2k_BT\left(-\frac{V_{2t}\bar{\rho}}{k_BT} + 1 - \frac{1}{6}A_{2t} + \frac{5}{32}A_{2t}^2\right), \quad (10)$$

where

$$V_{2t} = \frac{2V_{2ta}+V_{2tb}}{3},$$

$$V_{2ta} = -\int\int W(X,Y)\cos(qX)\cos\left(\frac{qY}{\sqrt{3}}\right)dXdY,$$

$$V_{2tb} = -\int\int W(X,Y)\cos\left(\frac{2qY}{\sqrt{3}}\right)dXdY. \quad (11)$$

Differentiating F by A_{2t} gives extrema at

$$A_{2t}=0, \quad \frac{2}{5}\left(1 \pm \sqrt{-19+20\frac{\bar{\rho}V_{2t}}{k_BT}}\right). \quad (12)$$

At nonzero modulation A_{2t} is real, so the following is the necessary condition for the existence of the triangular structure:

$$\frac{\bar{\rho}V_{2t}}{k_BT} \geq \frac{19}{20}. \quad (13)$$

Meanwhile, if

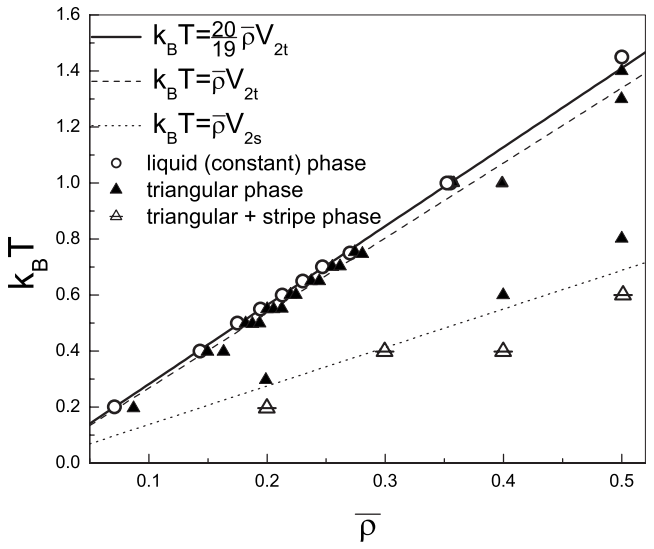

FIG. 1. Phase diagram of single-component system in two dimensions. The analytic solutions for the solidus, liquidus, and triangle/stripe lines are made by one-mode approximation as in Sec. II A and are compared with numerical calculations (points) as in Sec. III.

$$\frac{19}{20} \leq \frac{\bar{\rho}V_{2t}}{k_B T} \leq 1, \tag{14}$$

$\Delta F/a^2\bar{\rho}$ in Eq. (10) has local minima at $A_{2t}=0$ and $A_{2t}=\frac{2}{5}(1+\sqrt{-19+20\bar{\rho}V_{2t}/k_BT})$. Therefore in this range, constant phase (i.e., $A_{2t}=0$) and triangular phase can coexist. The solidus line can be obtained from Maxwell's equal-area construction or the equal tangent rule. From equal tangent rule, the solidus line reads $k_BT=\frac{20}{19}\bar{\rho}V_{2t}$.

Figure 1 is the phase diagram of two-dimensional structures driven by one-mode approximations as described above. The liquidus and solidus are made by the equations $k_BT=\frac{20}{19}\bar{\rho}V_{2t}$ and $k_BT=\bar{\rho}V_{2t}$, respectively, and the numerical calculations are presented as points. Here and throughout this paper, as for the pair potential $W(\vec{r},\vec{r}')$ in Eqs. (8), (9), and (11) and the numerical test, a modified Lennard-Jones pair potential is used (see Fig. 2). The description about this potential is found in Sec. III. The linearity of solidus and liquidus lines also appears in experimental studies on the solid state of inert atoms.[7] Even though we do not present the results of either the microstructure or the free energy here, they show the same simulation results not only on the liquidus or solidus lines but also whenever the systems have the same values of $\bar{\rho}/k_BT$. The numerical simulation method of the temporal evolution of atomic density is described in the following sections.

B. Dynamics

In this work, the microstructure evolution, described by the atomic density evolution, is assumed to be dissipative and driven by free-energy minimization. The kinetic equation for this conserved field $\rho(\vec{r})$ is

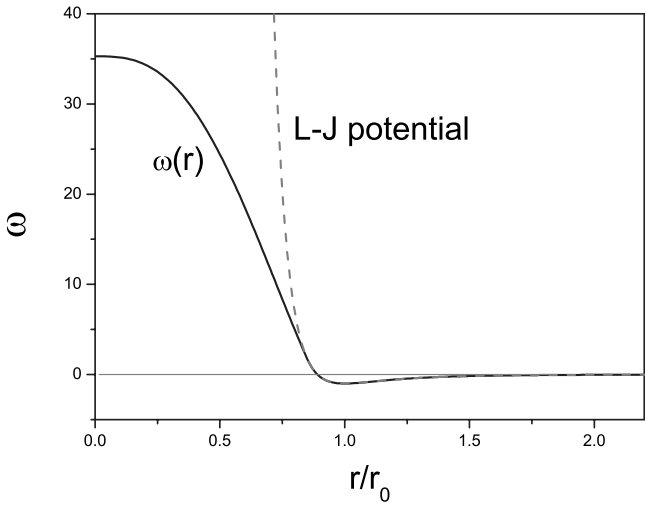

FIG. 2. Example of pair potential $w(|\vec{r}-\vec{r}'|)$ [Eq. (17)] used for the two-point correlation function of Eq. (1). The potential presented in the figure is third order polynomial form where the coefficients satisfy Eq. 18.

$$\frac{\partial \rho}{\partial \tau} = \nabla\left(M\,\nabla\,\frac{\delta F}{\delta \rho}\right) + \eta, \tag{15}$$

where M is the mobility matrix and η is the noise from thermal fluctuation. In this work, mobility is considered as a constant and thermal fluctuation is zero. From Eqs. (1) and (15), the kinetic equation of $d(\vec{r},t)$ is derived as following:

$$\frac{\partial d(\vec{x})}{\partial \tau} = \tilde{\nabla}^2\left[\int \bar{\rho}\omega(\vec{x},\vec{x}')d(\vec{x}')d\vec{x}' + T^*\left(d(\vec{x}) - \frac{1}{2}d(\vec{x})^2 + \frac{1}{3}d(\vec{x})^3\right)\right]. \tag{16}$$

Here the dimensionless variables are $\vec{x}=\vec{r}/r_0$, $\omega=W/W_0$, $T^*=k_BT/W_0$, and $\tau=tMW_0/r_0^2$, where $W_0=W(r_0)$.

III. COMPUTER SIMULATION

In this section, we show several applications of isothermal microstructure evolutions of a single-component, two-dimensional, periodic boundary system by solving the kinetic equation [i.e., Eq. (16)] of reduced atomic density $d(\vec{r},t)$. The differential equation is solved in real space and the fully explicit Euler discretization method is used. All Laplacians are calculated using the "spherical Laplacian" as in Refs. 2 and 20 and the grid size used in this method is $\Delta x=0.2$. The time step is automatically adjusted at each time by the maximum value of the right-hand side of Eq. (16). For the interatomic potential, we use Lennard-Jones potential with a "softened" core and truncated outside

$$\omega(r) = \begin{cases} 1/r^{12} - 2/r^6 \equiv \omega_{\mathrm{LJ}}(r), & r_{\mathrm{in}} < r < r_{\mathrm{out}} \\ 0, & r \geq r_{\mathrm{out}} \\ \omega_{\mathrm{in}}(r), & r \leq r_{\mathrm{in}}, \end{cases} \tag{17}$$

where r is reduced distance with respect to r_0, where $dW/dr|_{r_0}=0$. As for the softened core potential $\omega_{\mathrm{in}}(r)$ we use

a function which satisfies the conditions as below:

$$\omega_{\text{in}}(r_{\text{in}}) = \omega_{\text{LJ}}(r_{\text{in}}),$$

$$\omega'_{\text{in}}(r)|_{r=r_{\text{in}}} = \omega'_{\text{LJ}}(r)|_{r=r_{\text{in}}}, \tag{18}$$

$$\omega'_{\text{in}}(r)|_{r=0} = 0,$$

$$V_1, V_{2s}, V_{2t}, \ldots > 0.$$

While the pair-correlation function from ADF and PFC methods is periodic or oscillating at $r>1$ when it transforms to real space, the pair potential in this work is maintained with a nonoscillating tail. Figure 2 shows an example of $\omega(r)$ for the case of $r_{\text{in}}=0.85$ and $r_{\text{out}}=4$. This $\omega(r)$ gives V_1, V_{2s}, and V_{2t} as 1.986, 1.376, and 2.679, respectively. For computer simulations in this study, we use these r_{in} and r_{out} values for $\omega(r)$. The modification of $\omega(r)$, where $r<r_{\text{in}}$ reduces the "self-repulsion," since $\rho(\vec{r})$ and $\rho(\vec{r}+\vec{r}')$, especially where $|\vec{r}'|<r_{\text{in}}$, can be considered as the densities of the same atom. The "softening" of the repulsive part of the interatomic potential or pair-correlation function also has been studied in DFT papers.[18,19]

In the subsections following, we discuss the computer simulation results of solidification, grain growth, and annealing. The simulation conditions are all the same as mentioned above, except the initial conditions of each systems and T^*. As briefly mentioned previously, the simulation results are the same when $T^*/\bar{\rho}$ are the same, so we do not consider the result with different r conditions.

A. Solidification in two dimensions

In this section, we present simulations of two-dimensional solidification of single-component systems. Two types of samples are prepared: one sample (sample A-I) is a liquid phase with Gaussian noise of $0.1A_{2t}$ [see Eq. (12)]; the other one (sample A-II) has the same liquid structure as the sample A-I, but has nuclei of a triangular structure dispersed in the liquid. Each nucleus has a diameter of about eight atoms, and the initial amplitude of the density wave is set at A_{2t}. In this case the solidification is heterogeneous and occurs mainly at the phase boundary. In both cases, $T^*=0.5$ and $\bar{\rho}=0.2$, and these conditions are below the solidus in Fig. 1.

Figures 3(a) and 3(b) show the time evolution of density and free-energy difference in terms of $\langle|d|\rangle$ and $F^*=\Delta F/a^2\bar{\rho}$, respectively. Below the solidus the periodic density is favored, therefore the overall directions of evolution are increased in density and decreased in free energy accordingly. However, the evolution rate is different in time, showing "S" curve. In early times, the $\langle|d|\rangle$ increase and F^* decrease are slow. In this stage, in the liquid phase, sites with large density induce the other sites around them (i.e., with distance r_0) and the induced modulation makes further density modulations. Even though the pair potential we use in this work is not periodic, this chain reaction gives the periodic nature to the "effective" potential as the density modulation evolves. Yet the amplitude of the density modulation is not large enough, this "selecting and fostering" the density

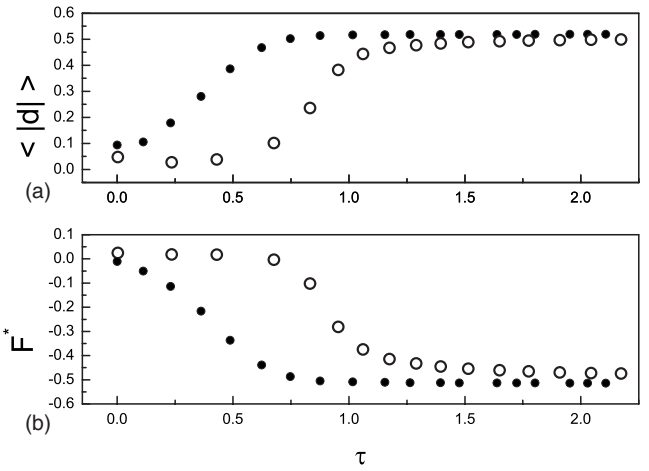

FIG. 3. Density and free-energy evolutions in solidification represented as $\langle|d|\rangle$ on (a) and F^* on (b), respectively. Open circles indicate sample A-I, i.e., supercooled liquid with Gaussian noise; solid circles indicate sample A-II, i.e., sample A-I with nuclei of diameter of eight atoms. τ is reduced time unit.

modulation is weak. Moreover, since the periodic density wave has short-range order, as shown in Fig. 4(a), the enhancement by the resonance with the "neighbor atoms" is weak. If there are heterogeneous sites, as in sample A-II, however, the large gradient of free energy at the phase boundary initiates and drives the density wave into the liquid phase. Figures 5(a) and 5(c) show the planar density wave around the nuclei. While the amplitude of the density wave grows, the evolution rates of $\langle|d|\rangle$ and F^* accelerate. As compared at Fig. 3, this rapid evolution stage starts later in sample A-I than in A-II, but the slope is larger in the former case. Figures 4(a) and 5(c) correspond to the initiation of the second stage of samples A-I and A-II, respectively. In both cases, regardless of the size, there are small grains (i.e., periodic density wave with the amplitude of A_{2t}). Note that

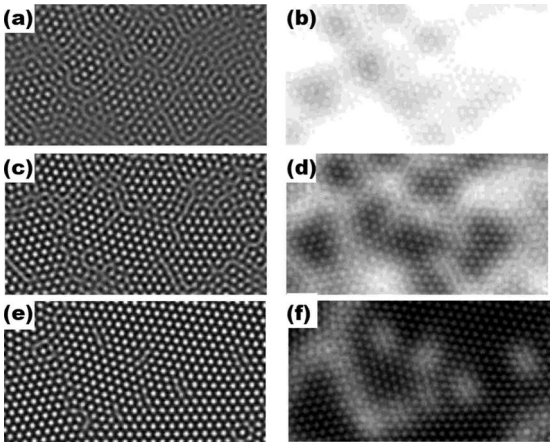

FIG. 4. Density (left three) and free-energy (right three) maps of sample A-I of Sec. III A. Brighter shade corresponds to atomic positions in the density maps and larger free energy in free-energy map. The snapshots are taken at [(a) and (b)] $\tau=0.27$, [(c) and (d)] $\tau=0.82$, and [(e) and (f)] $\tau=1.05$, respectively. The free energy is smoothed by averaging the free energy in $r<r_{\text{out}}$ range.

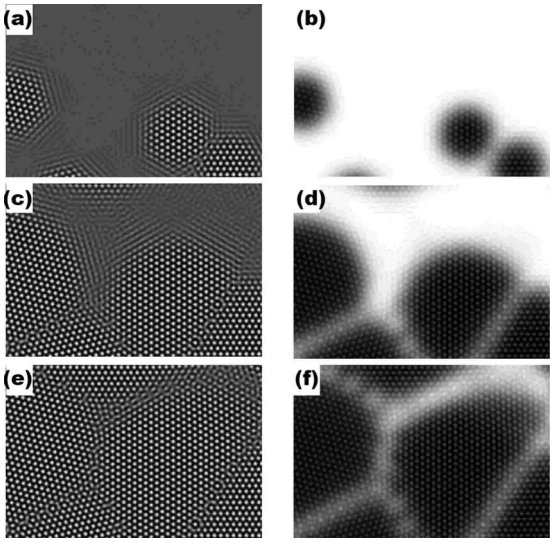

FIG. 5. Density (left three) and free-energy (right three) maps of sample A-II of Sec. III A. Brighter shade corresponds to atomic positions in the density maps and larger free energy in free-energy map. The snapshots are taken at [(a) and (b)] $\tau=0.15$, [(c) and (d)] $\tau=0.27$, and [(e) and (f)] $\tau=0.57$, respectively.

while the effect of the second term of the right-hand side of Eq. (1) is smaller than the first term, larger density enhances more density modulations at the preferred sites. After the density modulations reach to its A_{2t} in most of the samples [see Figs. 4(e) and 5(e)], the evolution rate decreases. In this stage, grains meet the other grains, and long-range order is achieved in long time by rearranging the density wave in space. This corresponds to dislocation and/or grain-boundary migration. Figure 6 shows the free-energy maps of samples A-I (a) and A-II (b) at $\tau=2.5$. Despite $\bar{\rho}$ and T^* being the same for the two samples, the microstructures are quite different in terms of the grain size and its distribution, grain-boundary types, and dislocations trapped inside the grain. We discuss further evolution in the section following.

B. Grain growth

Grain growth is made by the motions of grain boundaries and their junctions. The driving force of those motions is a function of grain-boundary energy, which is decided automatically from the pair potential "W" in this study. In this section we present the phenomenological results of grain growth, i.e., the motion of grain boundaries and their junctions, and discuss the effect of the grain-boundary energies.

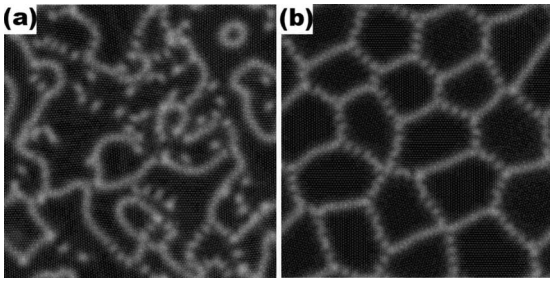

FIG. 6. Free-energy maps of (a) sample A-I (initial liquid structure has no initial nuclei) and (b) A-II (started from liquid phase with nuclei), respectively. Both simulation is performed under the conditions of $T^*=0.5$ and $\bar{\rho}=0.2$, and the figure are taken at $\tau=2.5$. The free energy is smoothened by averaging the free energy in $r<r_{\text{out}}$ range.

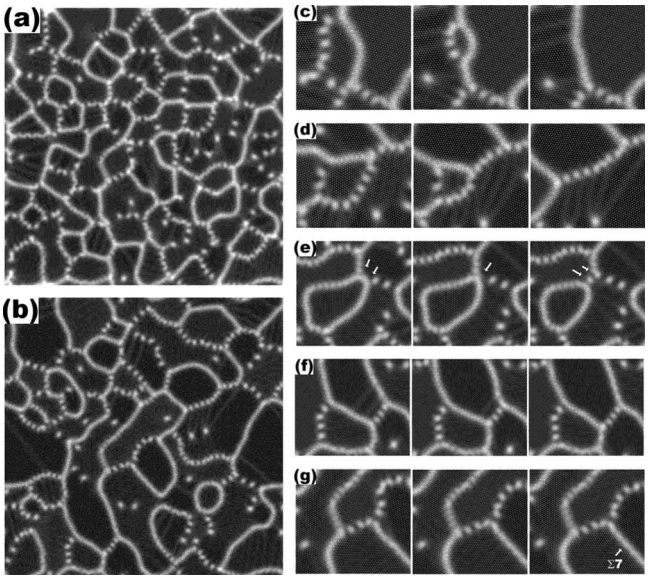

FIG. 7. Free-energy maps of polycrystalline samples with conditions of $T^*=0.5$ and $\bar{\rho}=0.2$. (a) is a sample with 100 grains of random size and crystallographic distributions and (b) is after $\tau=265$. (c)–(g) show snapshots of part of the sample; (c) grain adjacent to two grains (from left $\tau=40$, $\tau=80$, and $\tau=100$); (d) grain adjacent to four grains (from left $\tau=40$, $\tau=100$, and $\tau=200$); (e) two triple junctions (at $\tau=40$) merging into one quadrijunction (at $\tau=80$) and split into two triple junctions (at $\tau=100$); (f) triple junctions with one low angle and two high angle grain boundaries each (from left $\tau=100$, $\tau=200$, and $\tau=260$); (g) triple junctions with high angle and coincident site lattice grain boundaries each (from left $\tau=100$, $\tau=200$, and $\tau=260$).

The initial structure is shown in Fig. 7(a). It is a polycrystalline sample which has 100 grains with random sizes and crystallographic directions. The sample is kept under the conditions of $T^*=0.5$ and $\bar{\rho}=0.2$ until $\tau=260$ [Fig. 7(b)]. As shown in Fig. 7(a), the starting structure has many flat grain boundaries. Since grain-boundary motion during grain growth is controlled by the grain-boundary curvature, i.e., the lower the curvature, the lower the driving force, the driving force of the grain growth of our initial system mostly comes from the grain-boundary junction. The grain-boundary energy is a function of the crystallographic directions of the adjoining grains. In this study, we do not calculate the grain-boundary energies but assume that they follow what is known. That is, low angle grain boundary (up to $10°-15°$, shown as dotted line or row of dislocations in the figure) has low energy with increasing value with angle, while high angle grain boundary (shown as solid line in the figure) has high energy unless it is a coincidence site lattice boundary, i.e., $\Sigma 7$ (21.8°), $\Sigma 13$ (27.8°), or $\Sigma 19$ (13.2°). With this assumption, the equilibrium condition of grain boundaries at the triple junction is determined as $\gamma_i/\sin\alpha_i=\text{const}$, where γ_i is the energy of grain boundary and α_i is its dihedral angle at the junction. The grain boundaries of Fig. 7(a)

are incidental and do not meet this equilibrium condition yet. Therefore the triple junctions migrate toward the equilibrium condition, which then causes the grain-boundary curvature increase. The driving force to straighten the boundaries competes with that of triple junction motion while the grain boundaries and their junctions move together. Figures 7(c) and 7(d) show the snapshots of motion of the grain boundaries and triple junction. In both cases grains shrink and disappear, not by grain merging, but by grain boundary and triple junction migration to merge. There also exist quadrijunctions initially and in the middle of grain growth. Quadrijunction is energetically unfavorable compared with two triple junctions in general, so it tends to split into two triple junctions. The direction it splits depends on the dihedral angles at the junction and the energy of the grain boundary newly formed from the splitting. It is also possible that two triple junctions form a quadrijunction to split into two triple junctions in different directions. Figure 7(e) shows the case that two triple junctions, lying on high energy grain boundary, merged temporarily into a quadrijunction and then split into two triple junctions and a low energy grain boundary. After these migrations, the local equilibrium of polycrystalline sample spreads out and the motion of dislocations and their junction slows down. In Fig. 7(f), the triple junctions, made by one low angle and two high angle grain boundaries each, show a reasonable equilibrium angle. Figure 7(g) shows two interesting triple junctions: the one on the left has a high angle and two low angle grain boundaries and the dihedral angle of the high angle boundary is close to 90°; the other triple junction is composed of two low angles and one coincidence site lattice boundary and all the dihedral angles are close to 120°.

C. Annealing

In this section, the simulation results of annealing process are presented. The starting polycrystal of the sample is composed of 20 single-crystal grains of triangular structure with four different directions (15°, 30°, 45°, and 60°, relatively) and are treated in different temperature conditions $T^*=0.5$ (sample C-I), $T^*=0.55$ (sample C-II), and $T^*=0.56$ (sample C-III) for comparison. When the treatment temperature is above $T^*=0.57$, the modulated density decreases its amplitude and disappears within $\tau<0.1$. Figure 8 shows the snapshots of free energy indicating the microstructural evolution with time: from the leftmost column, samples C-I, C-II, and C-III, respectively; from the uppermost row, averaged free energy at $\tau=5$, 15, and 25, respectively, and the figures in the lowermost row present atomic density of the boxed portion of free-energy maps at $\tau=25$. The conditions of samples C-II and C-III are both below the liquidus and above the solidus, but their microstructure evolves in different ways from each other. But in sample C-II, according to the free-energy maps of the microstructure [i.e., (b), (e), (h), and (k) in Fig. 8], neither the broadening of the grain boundary nor the liquid phase is shown except at the grain-boundary junctions. The microstructural evolution is faster and noticeable than sample C-I within the same time range. The number of high energy grain-boundary junctions, such as quadruple junctions, decreases with time by separating into two triple junctions. Comparing the microstructure of sample C-I, at higher temperature ($T^*=0.55$, sample C-II) the grain boundary remained with curve depending on the types of the grain boundaries at the junctions (see the snapshots of the middle column in Fig. 8), while at the lower temperature ($T^*=0.5$, sample C-I) grain boundaries are straighter and sharper (see the left column of Fig. 8). When we compare the atomic density maps [i.e., Figs. 8(j)–8(l)], the modulation of the atomic density at the defect sites is smeared out at higher temperature. In sample C-III, the grain boundary, or where the density modulation is not periodic, widens and the grains become more round (see rightmost column in Fig. 8). The smaller crystals disappear faster while the larger crystal grows by consuming smaller crystals. This directional rearrangement occurs comparably fast by the grain-boundary "melting" and "recrystallizing." This is different from melting (above $T^*=0.57$), where the all the grains dissolve and disappear. The density of the bright parts in Figs. 8(c), 8(f), and 8(i) is slightly lower than zero, which indicates that this region is liquid. Note that $\bar{\rho}$ is the average density of the triangular state of A-II and B-II, and the average density of

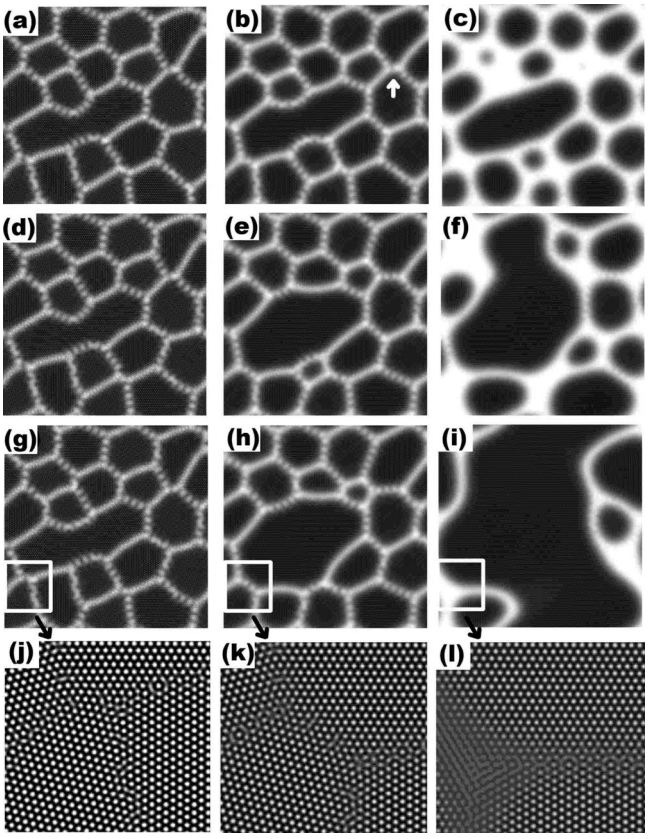

FIG. 8. Free-energy maps of annealed polycrystalline samples. From the leftmost column, $T^*=0.5$ (sample C-I), $T^*=0.55$ (sample C-II), and $T^*=0.56$ (sample C-III), respectively; from the top row, averaged energy at $\tau=0.5$, $\tau=1.5$, and $\tau=2.5$, respectively, and atomic density (boxed area in energy maps at $\tau=2.5$). The free energy is smoothed by averaging the free energy in $r<r_{\text{out}}$ range. Higher F^* is presented as brighter color, and the brightness of each temperature conditions is adjusted to contrast the high energy sites (i.e., dislocations and grain boundaries).

liquid at equilibrium (not the constant density or supercooled liquid) is lower than $\bar{\rho}=0.2$. What is interesting is that the grain growth occurs faster at higher temperature even though the mobility is set to be constant (not a function of temperature). As exemplified in Eq. (12) for the triangular array, the higher the temperature, the smaller the amplitude of the density wave. This corresponds to larger "overlapping of neighboring atoms" which causes larger interactions between "atoms." More investigation about the temperature dependence of mobility will be made in other paper.

IV. CONCLUSION

A numerical approach using atomic density was presented for the simulation of microstructural evolution of materials. The temporal evolution of atomic density is driven by the free-energy relaxation, and in this paper the free-energy functional is defined by introducing a pair potential with softened core, satisfying the conditions for instability of atomic density modulation. Based on the phase diagram made by the approach suggested, numerical simulations, such as solidification, grain growth, and annealing process, were performed for one-component two-dimensional systems. Results tested in various conditions showed that atomic density modulation described well both the periodic and nonperiodic natures of microstructure phenomenologically.

ACKNOWLEDGMENT

The authors acknowledge support from the DOE OBES, Division of Materials Sciences, under Grant No. DE-FG02-06ER46336.

*jiheekim@rci.rutgers.edu

[1] K. R. Elder, M. Katakowski, M. Haataja, and M. Grant, Phys. Rev. Lett. **88**, 245701 (2002).
[2] K. R. Elder and M. Grant, Phys. Rev. E **70**, 051605 (2004).
[3] P. Stefanovic, M. Haataja, and N. Provatas, Phys. Rev. Lett. **96**, 225504 (2006).
[4] J. Berry, M. Grant, and K. R. Elder, Phys. Rev. E **73**, 031609 (2006).
[5] C. V. Achim, M. Karttunen, K. R. Elder, E. Granato, T. Ala-Nissila, and S. C. Ying, Phys. Rev. E **74**, 021104 (2006).
[6] K. A. Wu and A. Karma, Phys. Rev. B **76**, 184107 (2007).
[7] K. R. Elder, N. Provatas, J. Berry, P. Stefanovic, and M. Grant, Phys. Rev. B **75**, 064107 (2007).
[8] S. Majaniemi and M. Grant, Phys. Rev. B **75**, 054301 (2007).
[9] N. Provatas, J. A. Dantzig, B. Athreya, P. Chan, P. Stefanovic, N. Goldenfeld, and K. R. Elder, JOM **59**, 83 (2007).
[10] N. Goldenfeld, B. P. Athreya, and J. A. Dantzig, Phys. Rev. E **72**, 020601(R) (2005).
[11] B. P. Athreya, N. Goldenfeld, and J. A. Dantzig, Phys. Rev. E **74**, 011601 (2006).
[12] R. Backofen, A. Rätz, and A. Voigt, Philos. Mag. Lett. **87**, 813 (2007).
[13] Y. M. Jin and A. G. Khachaturyan, J. Appl. Phys. **100**, 013519 (2006).
[14] L.-Q. Chen and A. G. Khachaturyan, Acta Metall. Mater. **39**, 2533 (1991).
[15] L.-Q. Chen and A. G. Khachaturyan, Phys. Rev. B **46**, 5899 (1992).
[16] L.-Q. Chen and A. G. Khachaturyan, Philos. Mag. Lett. **65**, 15 (1992).
[17] T. V. Ramakrishnan and M. Yussouff, Phys. Rev. B **19**, 2775 (1979).
[18] S. van Teeffelen, C. N. Likos, N. Hoffmann, and H. Löwen, Europhys. Lett. **75**, 583 (2006).
[19] J. D. Weeks, D. Chandler, and H. C. Andersen, J. Chem. Phys. **54**, 5237 (1971).
[20] J. Hoppe and S. Yau, Commun. Math. Phys. **195**, 67 (1998).